Article

Efficient Combination of Carbon Quantum Dots and BiVO$_4$ for Significantly Enhanced Photocatalytic Activities

Chenyan Hu [1,†], Qingdi Chen [1,†], Maosheng Tian [1], Weiwen Wang [2], Junxia Yu [1] and Lianguo Chen [3,*]

1 School of Chemistry and Environmental Engineering, Wuhan Institute of Technology, Wuhan 430072, China
2 Institute for Environmental and Climate Research, Jinan University, Guangzhou 511443, China
3 State Key Laboratory of Freshwater Ecology and Biotechnology, Institute of Hydrobiology, Chinese Academy of Sciences, Wuhan 430072, China
* Correspondence: lchenam@ihb.ac.cn; Tel.: +86-27-68780042
† These authors contributed equally to this work.

Abstract: The development of highly efficient and stable photocatalysts is of critical importance for the removal of environmental pollutants, such as paraben preservatives. In this work, carbon quantum dots (CQDs) were used to modify bismuth vanadate (BiVO$_4$) through a hydrothermal reaction. Regarding the as-formed CQDs/BiVO$_4$ composite, TEM, XPS, and Raman spectra analysis demonstrated the strong interaction between CQDs and BiVO$_4$, possibly leading to the elevated energy level of the composite. As compared to pristine BiVO$_4$, CQDs/BiVO$_4$ showed an increase in light harvesting, and significantly enhanced visible-light activities in degrading the typical paraben pollutant—benzyl paraben (BzP)—where the maximum 85.4% of BzP was degraded in 150 min. After four cycle reactions, the optimum sample 0.6%CQDs/BiVO$_4$ still degraded 78.2% of BzP, indicating the good stability and reusability of the composite. The notably higher photocurrent and smaller arc in Nyquist plot were measured by CQDs/BiVO$_4$, unveiling the improved photocharge separation and lowered interfacial charge transfer resistance by CQDs modification. Meanwhile, due to the promoted energy level, CQDs/BiVO$_4$ practically produced $\bullet O_2^-$ species and thereby contributed to the BzP degradation, while they had no ability to produce $\bullet OH$. This was contrary to the BiVO$_4$ system, where $\bullet OH$ and h^+ played the dominant roles.

Keywords: carbon quantum dots; BiVO$_4$; paraben preservatives; photocatalytic degradation

1. Introduction

Photocatalysis has been recognized as one of the most promising technologies in solar fuel production and contaminant removal due to its low cost, environmental friendliness, and easy operation. In principle, an efficient photocatalytic reaction necessitates the catalyst possessing excellent light absorption, fast photocharge separation and transfer, as well as high redox potentials. Among the numerously developed semiconductor photocatalysts, monoclinic scheelite bismuth vanadate (BiVO$_4$) is particularly noteworthy because it is inexpensive, environmentally benign, chemically stable, and visible-light responsive ($E_g \approx 2.4$ eV). Moreover, its valance band (VB) is located considerably high, which enables the generation of powerful reactive species, such as hydroxyl radical ($\bullet OH$) [1]. However, pristine BiVO$_4$ suffers from poor charge transport and resultant rapid recombination of photogenerated electron–hole pairs [2]. To ameliorate the photocatalytic properties of BiVO$_4$, various strategies have been explored, including impurity doping [3], co-catalysts loading [4], and heterojunction assembly [5].

As a new member of carbon-based nanomaterials, carbon quantum dots (CQDs) possess broad optical absorption, strong and tunable photoluminescence (PL) emissions, good biocompatibility, nontoxicity, and other attractive properties, thereby promising diverse applications in sensing, bioimaging, optoelectronics, catalysis, and energy conversion/storage since its first discovery in 2004 [6,7]. Meanwhile, CQDs have superior electron transfer and

reservoir abilities. When coupled with other photocatalysts, such as TiO_2, g-C_3N_4, $BiSbO_4$, and BiOCl, CQDs could not only broaden the spectral absorption, but also facilitate the photogenerated charge separate and transfer [8–11]. Nevertheless, few studies reported the incorporation of CQDs with $BiVO_4$, and generally attributed the improved photocatalytic degradation of rhodamine B and tetracycline to the enhanced charge separation and transport [12,13]. To further improve the photocatalytic activity of $BiVO_4$ by CQD modification, more understanding about light harvesting, charge separation, and transport, as well as electronic properties of the CQDs/$BiVO_4$ composite, is indispensably needed.

Parabens are a group of *p*-hydroxybenzoic acid esters, which are popularly used as preservatives in stuffed food, cosmetics, pharmaceuticals, and other personal care products [14]. With the globally augmented population and life quality in recent decades, paraben-contained products have been extensively consumed, leading to their widespread occurrence in diverse aqueous environments, including wastewater, surface water, ground water, and drinking water [15,16]. Meanwhile, considerately high concentrations of parabens have been detected in aquatic organisms and even human body samples, inferring their latent bioaccumulation and biomagnification [17,18]. However, recent toxicological studies evidenced that parabens had the potential to induce reproductive toxicity, developmental toxicity, hepatotoxicity, and neurotoxicity at environmentally realistic concentrations [19–22]. Therefore, it is highly urgent to develop an efficient method to remove parabens from water bodies.

Herein, with the aim of enhancing the photocatalytic activity of $BiVO_4$ by CQDs modification, a facile hydrothermal method has been explored to fabricate CQDs/$BiVO_4$ composites. Their visible-light photocatalytic abilities have been assessed by degrading benzyl paraben (BzP), which is a commonly used preservative of high toxicity concern [23]. With the assistance of physiochemical characterizations, photoelectrochemical measurements, and trapping agent tests, compositing with CQDs was disclosed to not only facilitate the charge separation of $BiVO_4$, but also elevate its energy level and consequently modulate the reactive species generation. As expected, significantly enhanced photocatalytic activity was observed over the optimum CQDs/$BiVO_4$ composite. Overall, this work made a profound study about the CQDs/$BiVO_4$ combination and their photocatalytic application, which provided more thoughts for photocatalyst design as well as the efficient removal of paraben pollutants.

2. Results and Discussion

2.1. Characterization of the Prepared Catalysts

In this work, CQDs/$BiVO_4$ composites were synthesized via a hydrothermal reaction. Based on the volume ratio of added CQDs solution (60 μL, 120 μL, and 300 μL) to the whole reaction solution, the prepared composites were referred as 0.3%CQDs/$BiVO_4$, 0.6%CQDs/$BiVO_4$, and 1.5%CQDs/$BiVO_4$, respectively, and their theoretical weight percents were 0.0025%, 0.005%, and 0.0125%. The phase structures of the as-synthesized CQDs, $BiVO_4$, and CQDs/$BiVO_4$ composite were examined by X-ray diffraction (XRD) analysis. As seen in Figure 1a, CQDs had a wide diffraction peak at 23.1°, assigned to (100) planes of their graphite constituents [24]. $BiVO_4$ and 0.6%CQDs/$BiVO_4$ depicted similar diffraction patterns, where the main diffraction peaks at 2θ values of 19.0°, 28.9°, 30.5°, 34.5°, 35.2°, 46.7°, 47.4°, and 53.4° related well with the (011), (121), (040), (200), (002), (240), (042), and (161) crystal planes of monoclinic scheelite $BiVO_4$ (JCPDS No. 14-0688) (space group 15, C^6_{2h}). The nonvisible CQDs peak in XRD pattern of 0.6%CQDs/$BiVO_4$ was potentially ascribed to their high dispersion and/or low content in the composite. The field emission scanning electron microscopy (FESEM) image showed that pristine $BiVO_4$ existed in a decagonal shape with smooth surface (Figure S1). The averaged particle thickness was 0.38 μm, and the length was in the range of 0.9–1.5 μm. After coupling with CQDs, $BiVO_4$ maintained its original morphology in CQDs/$BiVO_4$ (Figure 1b), while transmission electron microscope (TEM) elemental mapping evidenced the uniform distribution of C and N which could only be traced from CQDs in the composite (Figure 1c). The high-resolution

TEM (HRTEM) image of the composite visualized that a number of CQDs with a diameter smaller than 10 nm were evenly and intimately attached to $BiVO_4$ (Figure 1d). The different lattice spacings of 0.21 and 0.22 nm were characterized to (100) planes of CQDs and (121) planes of monoclinic $BiVO_4$ (Figure 1e), demonstrating their successful composition [25].
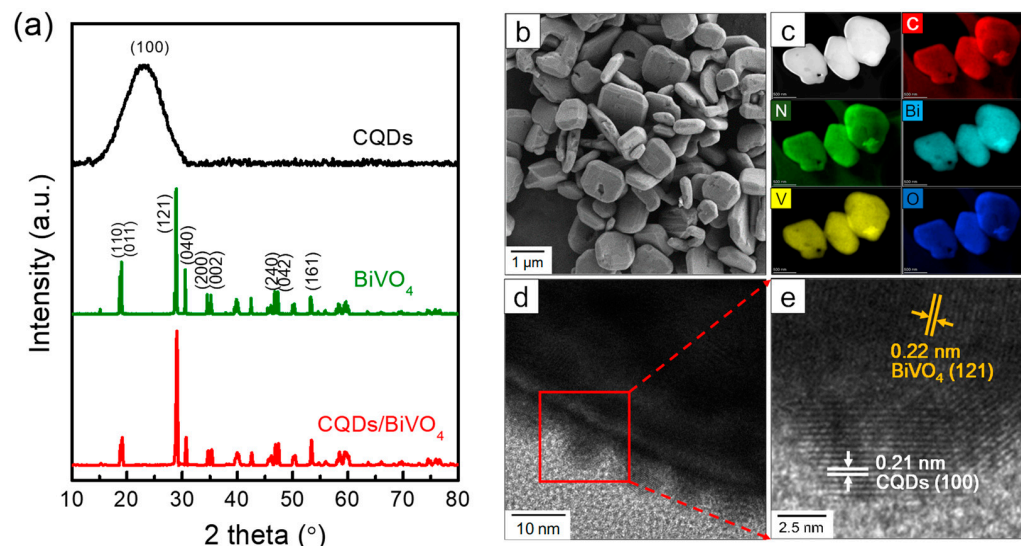

Figure 1. (**a**) XRD diffraction patterns of CQDs, $BiVO_4$, and 0.6%CQDs/$BiVO_4$. (**b**) FESEM image of 0.6%CQDs/$BiVO_4$. (**c**) TEM elemental mapping images of C, N, Bi, V and O; (**d**) HRTEM images of 0.6%CQDs/$BiVO_4$ and (**e**) the magnified image of selected area in (**d**).

Fourier transform infrared spectrascopy (FTIR) and Raman spectra were further recorded to clarify the constitution of the materials. As shown in Figure 2a, the IR spectrum of CQDs presented stretching vibrations at 3452 (O-H), 3246 (N-H), 2924 (C-H), 1655 (C=O), 1546 (C=N), and 1048 (C-O-C) cm^{-1}, while the peak centered at 1386 cm^{-1} was identified as the stretching vibration of C-N [26]. The IR peaks of $BiVO_4$ located at 746 and 810 cm^{-1} belonged to the symmetric and asymmetric stretching vibrations of VO_4^{3-} [27]. With respect to the IR spectrum of CQDs/$BiVO_4$, the peaks for CQDs (1386 cm^{-1}) and $BiVO_4$ (746 cm^{-1}) both appeared, thus validating their combination. Raman spectra analysis illustrated that CQDs had only a broad peak at 760–2300 cm^{-1} (Figure 2b), while the distinct D (disordered sp^2 carbon atoms) and G bands (conjugated sp^2 carbon atoms) were prominent in CQDs/$BiVO_4$ (inset of Figure 2b) [28]. The non-observed D or G band in CQDs possibly resulted from their high fluorescence (Figure S2) [29]. Pristine $BiVO_4$ displayed typical vibrational bands positioned at around 131, 215, 330, 372, 710, and 831 cm^{-1} [30]. After introducing CQDs, these characteristic Raman peaks of $BiVO_4$ slightly shifted towards lower frequencies, inferring the possible electron transfer at the CQDs/$BiVO_4$ interface.

The effect of the CQD combination on the surface electronic structure of $BiVO_4$ was mapped out by X-ray photoelectron spectroscopy (XPS). The survey spectra in Figure 3a manifests the existence of primary elements (C, N, Bi, V, O) in related CQDs, $BiVO_4$, and the CQDs/$BiVO_4$ composite. The peaks located at 1071 and 497 eV in the spectra of $BiVO_4$ and 0.6%CQDs/$BiVO_4$ corresponded to the Na 1s and its Auger electron energy, respectively. The existence of surface Na should be traced to the used NaOH during the synthesis process. The deconvolution of high-resolution C 1s spectra demonstrated the presence of C-C/C=C (284.6 eV), C-O/C-N (286 eV), and C=O (287.7 eV) in CQDs (Figure 3b) [31]. In comparison, the C-O/C-N peak of CQDs/$BiVO_4$ negatively shifted to 285.6 eV, while the C=O peak positively shifted to 288 eV. Here, using the binding energy of C-C/C=C at 284.6 eV as the reference for calibration may bring some uncertainty to the absolute binding energy of the elements in CQDs/$BiVO_4$. However, the opposite shift of C-O/C-N peak and C=O peak elucidates the chemical interaction between CQD and $BiVO_4$ reasonably. The N 1s

spectrum of CQDs was fitted into two peaks at 399.6 and 400.9 eV (Figure 3c), representing pyrrolic N and amino groups carrying hydrogen (NH_x) [24]. Due to the low N content, only pyrrolic N peak was deconvoluted in CQDs/BiVO$_4$ and negatively shifted to 399.4 eV. The broad peak located at 406.6 eV originated from the charging effect [32]. The Bi 4f spectrum of BiVO$_4$ presented two peaks at 158.4 and 163.6 eV (Figure 3d), and its V 2p spectrum had two peaks at 529.1 and 530.9 eV (Figure 3e), revealing the existence of the respective Bi^{3+} and V^{5+}. In the spectra of CQDs/BiVO$_4$, two Bi^{3+} peaks shifted to higher energies, whereas V^{5+} peaks conversely shifted to lower energies; this was possibly attributed to the changes in the surrounding chemical environment of Bi and V after the incorporation of CQDs [33]. The two divided O 1s peaks of BiVO$_4$ were attributed to lattice oxygen (O_L) at 529.1 eV and oxygen in the surface-absorbed hydroxyl group (OH^-) at 530.9 eV [34], which were both negatively shifted in CQDs/BiVO$_4$ (Figure 3f). These notably observed binding energy shifts of the elements in CQDs/BiVO$_4$ (C, N, Bi, V, and O) suggest a strong chemical interaction between CQDs and BiVO$_4$, in consistence with the Raman analysis.
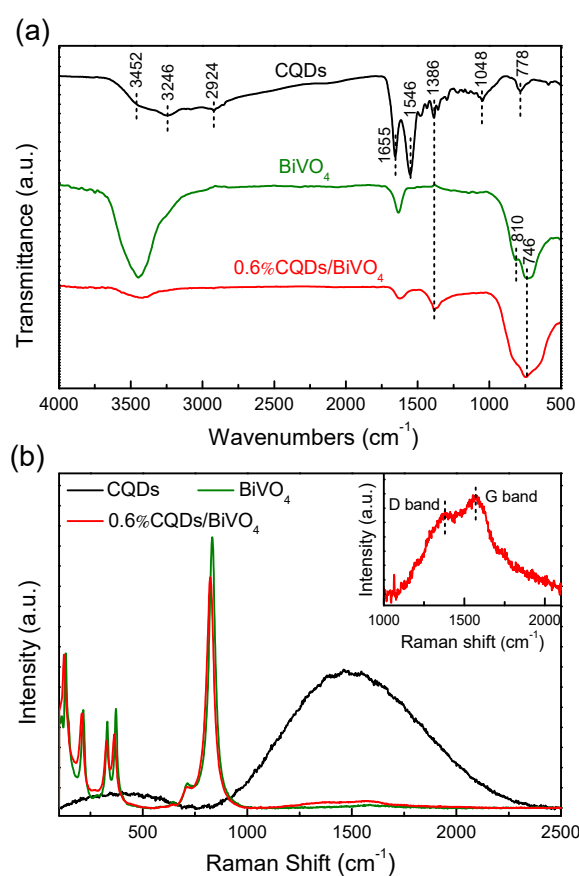

Figure 2. (**a**) FTIR spectra and (**b**) Raman spectra of CQDs, BiVO$_4$, and 0.6%CQDs/BiVO$_4$. Inset of (**b**) is the enlarged part of 0.6%CQDs/BiVO$_4$ at 1000–2100 cm^{-1}.

2.2. Optical Properties and Band Structure Estimation

The UV–vis absorption spectra were measured to probe the influence of CQDs on the optical property of BiVO$_4$. As shown in Figure 4a, BiVO$_4$ possessed a sharp absorption edge at approximately 520 nm. Comparatively, the synthesized CQDs/BiVO$_4$ composites exhibited noticeably enhanced visible-light harvesting as the CQDs amounts increased. Based on the equation: $\alpha h\nu = A(h\nu - E_g)^{n/2}$, where α, h, ν, A, and n represent the absorption coefficient, Planck constant, light frequency, proportionality constant, and the value of 4 for the indirect semiconductor, respectively, the band gap width of BiVO$_4$ was deduced to be 2.39 eV (Figure 4b), which is close to a previous report [35]. As the loading amount of CQDs was increased from 0.3%, 0.6%, to 1.5%, the band gap energies of the as-formed

CQDs/BiVO$_4$ composites were not affected much, showing a slight change from 2.39, 2.38, to 2.37 eV (Figure 4b).
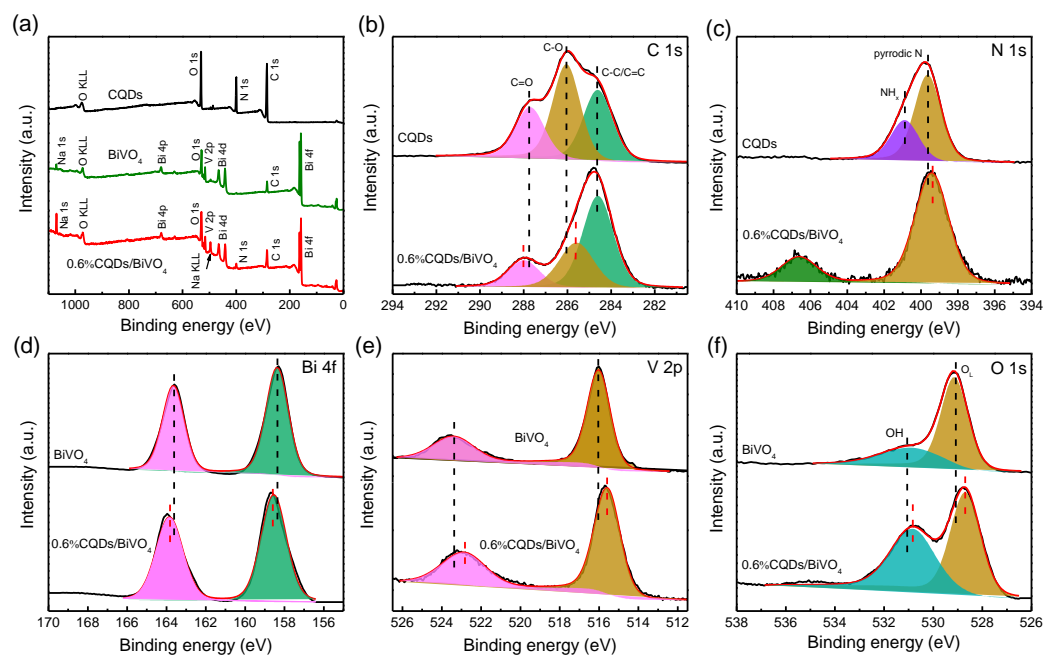
Figure 3. XPS survey spectra (**a**), high-resolution C 1s (**b**), N 1s (**c**), Bi 4f (**d**), V 2p (**e**), and O 1s (**f**) spectra of related CQDs, BiVO$_4$, and 0.6%CQDs/BiVO$_4$.
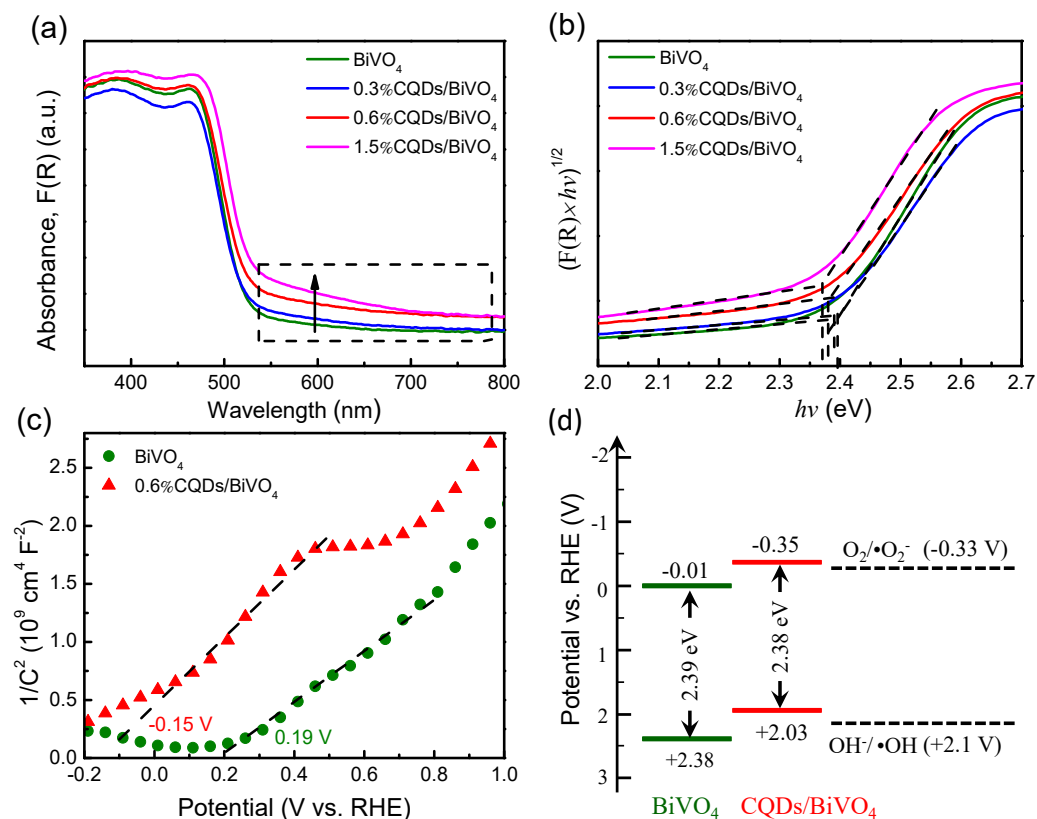
Figure 4. (**a**) UV–vis absorption spectra and (**b**) the corresponding Tauc plots of the as-synthesized BiVO$_4$ and CQDs/BiVO$_4$ composites with different CQDs amounts. (**c**) The Mott–Schottky plots and (**d**) estimated band structures of BiVO$_4$ and 0.6%CQDs/BiVO$_4$.

Further analysis by the Mott–Schottky plot (Figure 4c) illustrated that the flat band potential of $BiVO_4$ was located at +0.19 V vs. RHE, while the CQDs modification promoted the flat band potential of the composite more negative, namely, at −0.15 V vs. RHE. Here, the cause for the elevated flat band potential by CQDs is still unclear, but we suppose it is probably attributed to the aforementioned strong chemical bonding between CQDs and $BiVO_4$. Generally, in an n-type semiconductor, which is the case for $BiVO_4$, the conduction band (CB) potential is above the flat band potential at about 0.1–0.3 eV [35]. Thus, the CB potential of $BiVO_4$ and 0.6%CQDs/$BiVO_4$ was estimated to be −0.01 and −0.35 V vs. RHE. According to the equation: $E_{VB} = E_{CB} + E_g$, their VB potential was then calculated to be at +2.38 and +2.03 V vs. RHE. The estimated band structures of $BiVO_4$ and 0.6%CQDs/$BiVO_4$ were schemed in Figure 4d. Apparently, the CB and VB edges of pristine $BiVO_4$ were sited more positively than the corresponding potential of oxygen reduction ($O_2/\bullet O_2^-$, −0.33 V) and $\bullet$OH generation (+2.1 V), inferring that $BiVO_4$ was unable to produce $\bullet O_2^-$, but capable to yield $\bullet$OH. On the contrary, the CQDs/$BiVO_4$ composite exhibited a more negative CB band (−0.35 V) and VB band (+2.03 V), theoretically providing enough potential for $\bullet O_2^-$ generation but not enough for $\bullet$OH formation. The distinct energy structures and consequently differing reactive species between $BiVO_4$ and CQDs/$BiVO_4$ would presumably affect their photocatalytic performance.
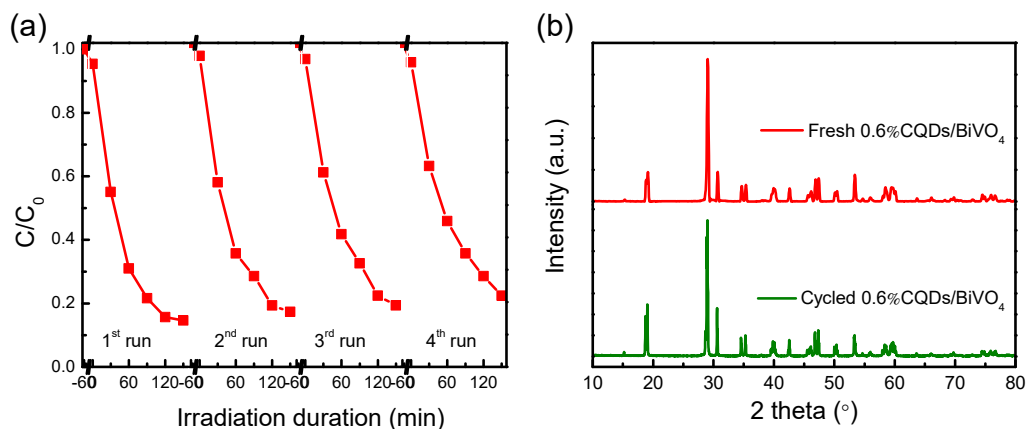
2.3. Photocatalytic Degradation of BzP over the as-Systhesized Catalysts

The prepared $BiVO_4$ and CQDs/$BiVO_4$ composites were then irradiated under visible-light (λ > 420 nm) to evaluate their photocatalytic activities in degrading BzP; the result is displayed in Figure 5. Without photocatalysts, the concentration of BzP changed slightly after irradiation for 150 min, indicating a negligible photolysis (Figure 5a). Due to the intrinsic limits (e.g., fast charge recombination), $BiVO_4$ gave rise to a moderate photocatalytic activity, only reaching a degradation efficiency of 47.8% at 150 min. After incorporation with CQDs, the obtained CQDs/$BiVO_4$ composites exhibited the pronouncedly improved photocatalytic efficiencies, where the optimal sample 0.6%CQDs/$BiVO_4$ degraded 85.4% of BzP. As a reference, the same amount of expanded graphite (EG), which was known to be another member of carbon materials but with larger morphology [36], was used to modify $BiVO_4$ by the same protocol. The obtained 0.6%EG/$BiVO_4$ showed the inferior photocatalytic enhancement to that of 0.6%CQDs/$BiVO_4$, emphasizing the critical role of CQDs in modifying the photocatalytic properties of $BiVO_4$. Meanwhile, the mechanically mixed sample (0.6%CQDs/$BiVO_4$(mixed)) showed moderately enhanced photocatalytic activity, presumably attributed to the low-quality interface that slowed down the charge separation as compared to the synthesized 0.6%CQDs/$BiVO_4$ composite. At a loading level beyond the optimum, the excessive CQDs in 1.5%CQDs/$BiVO_4$ might act as recombination centers and may consequently lead to a lowered degradation efficiency (72.1%) [12]. The kinetics of BzP degradation over $BiVO_4$ and CQDs/$BiVO_4$ composites revealed a good fitting with the first-order reaction dynamic (Figure 5b). The optimum sample (0.6%CQDs/$BiVO_4$) incurred the highest reaction rate (0.0189 min^{-1}), approximately 3.4 times as high as that of $BiVO_4$ (0.0055 min^{-1}).

For practical application, the stability and reusability of the CQDs/$BiVO_4$ composite was measured by cycling photocatalytic experiments. In Figure 6a, 78.2% of BzP was degraded after four cycled runs, which was only lower than the first run by 7.2%. The XRD patterns of the cycled photocatalyst and the fresh one are presented in Figure 6b. In comparison with the fresh sample, the crystal structure of the cycled 0.6%CQDs/$BiVO_4$ had no obvious change, which further confirmed its good stability and reusability.
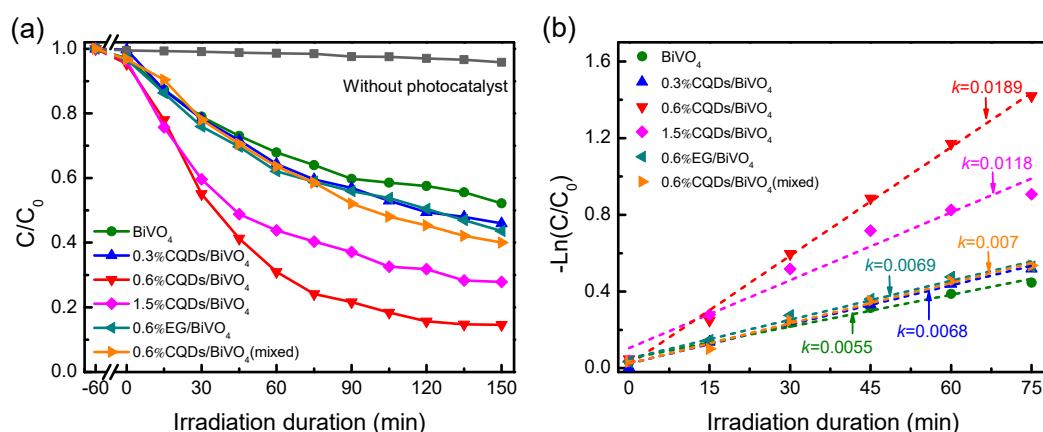
Figure 5. (**a**) Photocatalytic degradation of BzP over different catalysts under visible-light irradiation and (**b**) the corresponding first-order reaction kinetic plots.
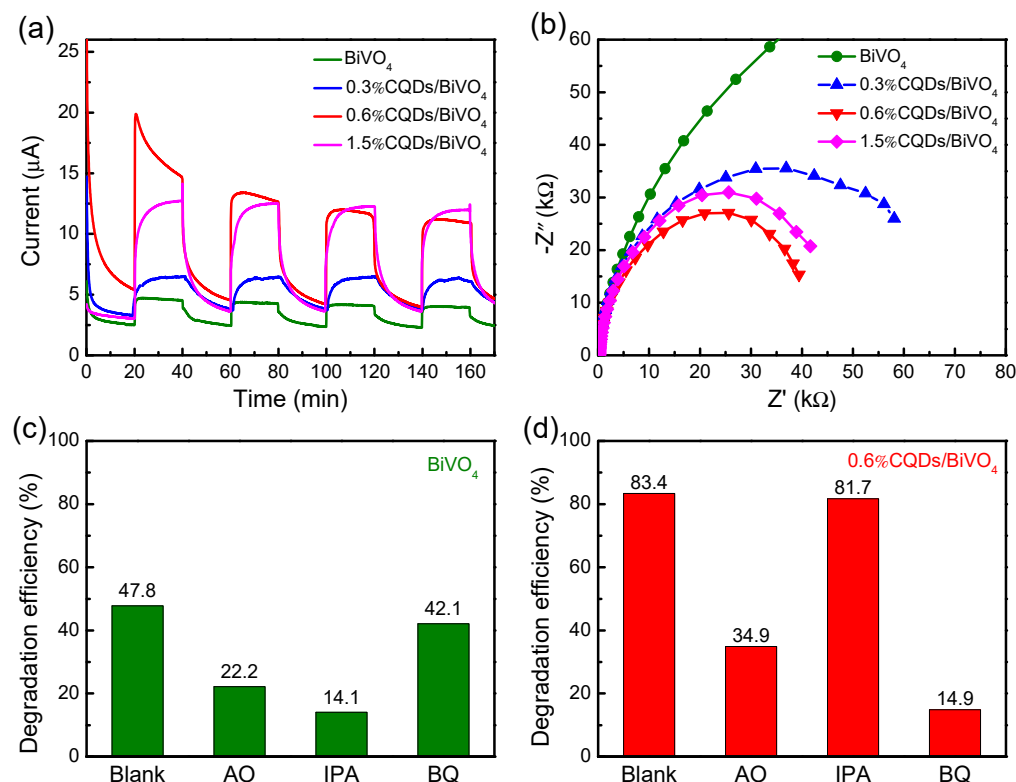

Figure 6. (**a**) Photocatalytic degradation of BzP over 0.6%CQDs/BiVO$_4$ composite in consecutive four cycles, and (**b**) XRD patterns of the used catalyst before and after the four cycles.

2.4. Insights into the Enhanced Photocatalytic Properties by CQD Modification

In order to get an insight into the mechanism of the photocatalytic enhancement, photoelectrochemical analysis was carried out to investigate the charge separation and transfer of BiVO$_4$ and CQDs/BiVO$_4$ composites. As seen from Figure 7a, CQDs/BiVO$_4$ composites generated higher photocurrents relative to pristine BiVO$_4$, demonstrating the improved charge separation by CQD modification. The highest photocurrent was generated by 0.6%CQDs/BiVO$_4$, nearly five-fold to that of BiVO$_4$. Concurrently, a weaker fluorescence was emitted by 0.6%CQDs/BiVO$_4$ (Figure S3). The lower PL intensity suggested the higher charge separation efficiency [37]. Therefore, the notable PL quenching of CQDs/BiVO$_4$ composite further testified its inhibited charge recombination by CQD modification, which thereby contributed to the improved photocatalytic properties. Moreover, the Nyquist plots of electrochemical impedance spectra (EIS) illustrated that CQDs/BiVO$_4$ composites had reduced interfacial charge transfer resistance, as signified by their smaller arc radii than that of BiVO$_4$ (Figure 7b).

Trapping experiments were further conducted to confirm the effects of reactive species on the photocatalytic degradation of BzP over BiVO$_4$ and CQDs/BiVO$_4$. Benzoquinone (BQ), isopropanol (IPA), and ammonium oxalate (AO) were employed as the trapping agents for $\bullet O_2{}^-$, $\bullet OH$, and h^+, respectively. In Figure 7c, the BzP degradation on BiVO$_4$ was reduced from 47.8% (no trapping agent) to 22.2% (AO), 14.1% (IPA), and 42.1% (BQ), indicating that the feasibly produced $\bullet OH$ played the dominate role in BzP degradation. The marginal effect induced by BQ implied that $\bullet O_2{}^-$ had a little effect on the degradation of BzP, which was presumably attributed to the lower CB potential of BiVO$_4$ than that

of $O_2/\bullet O_2^-$ (Figure 4d) [38]. By comparison, the addition of BQ substantially inhibited the BzP degradation over 0.6%CQDs/BiVO$_4$, demonstrating the enormous contribution of $\bullet O_2^-$ to BzP degradation. More importantly, this result confirmed the formation of $\bullet O_2^-$, which certified the elevated CB band of 0.6%CQDs/BiVO$_4$ by CQDs modification (Figure 4d). Consistently, the negligible effect induced by the trapping agent of IPA might be explained by the non-produced $\bullet OH$.


Figure 7. (**a**) Transient photocurrent responses and (**b**) EIS Nyquist plots of BiVO$_4$ and CQDs/BiVO$_4$ composites. The photocatalytic degradation of BzP over (**c**) BiVO$_4$ and (**d**) 0.6%CQDs/BiVO$_4$ at the presence of different trapping agents under visible-light irradiation for 150 min. Blank means that no trapping agent was added in the photocatalytic system.

Due to the low CB band position, BiVO$_4$ was hard to evolve H$_2$ without the assistance of a co-catalyst or bias [39]. In order to further prove the promoted energy level by CQDs modification, the photocatalytic H$_2$ evolution of BiVO$_4$, CQDs, 0.6%CQDs/BVO$_4$, as well as the mechanically mixed CQDs and BVO$_4$ (0.6%CQDs/BVO$_4$(mixed)) was performed under visible-light irradiation. Not surprisingly, no H$_2$ was evolved by BiVO$_4$ because its low CB band (-0.01 eV) could not provide enough overpotential for H$_2$ generation (Figure S4). Pure CQDs and low efficient 0.6%CQDs/BiVO$_4$(mixed) were not able to evolve the detectable H$_2$, neither. In contrast, 0.6%CQDs/BVO$_4$ produced 10.6 μmol/g$_{catalyst}$ of H$_2$ within 180 min, corroborating the elevated CB position of the CQDs/BVO$_4$ composite sufficiently.

Based on the above analysis, the mechanism of the CQDs/BiVO$_4$ composite in enhancing photocatalytic activities was proposed and shown in Scheme 1. Upon irradiation, the visible-light-responsive BiVO$_4$ was excited. In terms of pristine BiVO$_4$, the photogenerated holes would oxide OH$^-$ to form $\bullet OH$, and were subsequently involved in the photocatalytic degradation of BzP. Due to its low CB band, no $\bullet O_2^-$ could be produced. When CQDs were introduced to combine with BiVO$_4$, the photogenerated electrons would be efficiently separated, transferred to CQDs, and then reacted with O$_2$ to generate high oxidative species $\bullet O_2^-$ for BzP degradation. The holes, in turn, migrated onto the BiVO$_4$ surface to oxidize the adsorbed BzP. In this case, CQDs not only facilitated the photocharge

separation of BiVO$_4$, but also tailored the reactive species, which incurred the final and significantly enhanced photocatalytic properties.
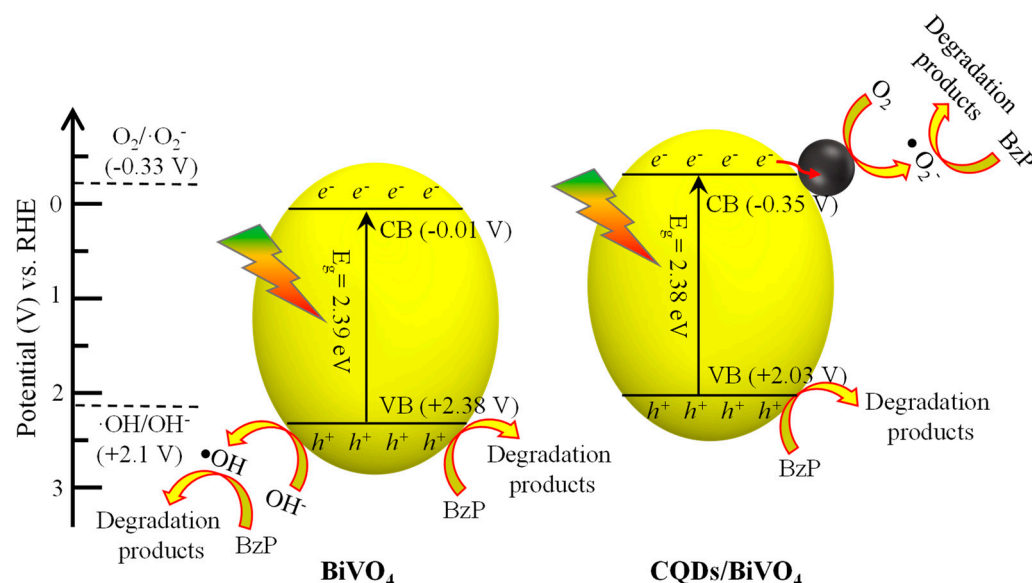
Scheme 1. Proposed photocatalytic mechanisms for BzP degradation over pristine BiVO$_4$ and the CQDs/BiVO$_4$ composite.

3. Materials and Methods

3.1. Chemicals

Ethanol absolute (99.7%), ammonium metavanadate (>99%), sodium hydroxide (96%), bismuth (III) nitrate pentahydrate (>98%), nitric acid (65~68%), citric acid (>99.5%), ethylenediamine (>99%), isopropanol (99.7%), and ethylene diamine tetraacetic acid (EDTA, >99.5%) were purchased from Sinopharm Chemical Reagent Co., Ltd. (Shanghai, China). Benzyl paraben (99%) was purchased from Macklin (Shanghai, China). Ammonium oxalate, benzoquinone, and Nafion (5 wt%) were obtained from Aldrich (Shanghai, China). Ultrapure water was used throughout this work.

3.2. Synthesis of CQDs, BiVO$_4$, and CQDs/BiVO$_4$

Carbon quantum dots (CQDs) were synthesized by using citric acid and ethylenediamine as precursors. Typically, 5 mmol of citric acid and 0.5 mL of ethylenediamine were dissolved in 10 mL of ultrapure water, which was then transferred into a 50 mL Teflon-lined autoclave and heated at 180 °C for 5 h. Upon cooling to room temperature, the obtained solution was centrifuged at 10,000 rpm for 15 min twice. The supernatant was taken as CQDs solution and stored at −4 °C for further use.

CQDs/BiVO$_4$ composites were synthesized via a hydrothermal method. Typically, different amounts of the CQDs solution (60 μL, 120 μL, and 300 μL) and 7.5 mL of ultrapure water were added into 2 mL of nitric acid containing 5 mmol of bismuth nitrate pentahydrate, and then dispersed under ultrasonic condition for 1 h to prepare solution A. Meanwhile, 5 mmol of ammonium metavanadate and 1 g of EDTA were dissolved in 10 mL of the NaOH solution (4 mol/L) under stirring to prepare solution B. Upon mixing solutions A and B, the pH of the mixture was adjusted to 7 by using NaOH and/or diluted nitric acid. Then, the mixture was poured into a 100 mL Teflon-lined autoclave and kept at 180 °C for 18 h. After the reaction, the as-obtained products were collected and washed with absolute ethanol and ultrapure water by centrifugation, and then dried at 60 °C overnight. According to the volume ratios of the added CQDs solution, the as-synthesized materials were named as 0.3%CQDs/BiVO$_4$, 0.6%CQDs/BiVO$_4$, and 1.5%CQDs/BiVO$_4$. Pure BiVO$_4$ was prepared as described above without the addition of the CQDs solution.

3.3. Characterization

The crystal structures of the as-prepared materials were confirmed by X-ray diffraction (XRD) on a Bruker D8 Advance with Cu $K\alpha$ at 40 kV and 40 mA as the radiation source. The field emission-scanning electron microscopy (FESEM) (ZEISS GeminiSEM 300) and transmission electron microscopy (TEM) (Talos F200S) were used to analyze the morphology of the materials. X-ray photoelectron spectroscopic (XPS) analysis was conducted on ThermoFischer ESCALAB 250Xi. All peak positions were calibrated against the C 1s at the binding energy of 284.6 eV. Fourier transform infrared (FTIR) spectra were measured on a Nicolet-6700 spectrometer (Thermo Electron, Waltham, MA, USA). Raman spectra were obtained from a DXR Raman microscopy system (Thermo Fisher, Waltham, MA, USA). The optical absorption performances of the as-prepared materials were characterized using a UV–Vis diffuse reflectance spectroscopy (DRS, Cary UV–Vis), where $BaSO_4$ was used as the background of the integrating sphere. Photoluminescence spectra were recorded by a Hitachi (F-700) spectrofluorophotometer.

3.4. Photocatalytic Degradation of BzP

The photocatalytic activities of these as-prepared materials were evaluated to degrade BzP. Specifically, 0.1 g of the catalyst was dispersed in a water-cooling reactor containing 100 mL of the BzP solution (10 mg/L). After stirring for 1 h in the dark to reach the adsorption–desorption equilibrium, the reactor was exposed to visible-light ($\lambda > 420$ nm) irradiated from a 300 W Xenon lamp (CEL HXF300) for 150 min. During the reaction period, 4 mL of the reaction solution was sampled every 15 min and filtered through a 0.22 μm polytetrafluoroethylene (PTFE) membrane. The concentration of BzP in the obtained filtrate was determined using a UV–Vis spectrophotometer (AOE in instrument, A590) at 256 nm. The photocatalytic efficiency was described as C/C_0, where C was the concentration of BzP at different times and C_0 was its initial concentration.

To test the stability and reusability of the photocatalyst, a four-cycled consecutive experiment was carried out. The used photocatalyst was centrifuged after each reaction, washed with ultrapure water several times, dried at 60 °C overnight, and then reused for the next degradation reaction.

Trapping agent experiments were carried out to investigate the main active species formed during the photocatalytic degradation of BzP by $BiVO_4$ and $CQDs/BiVO_4$. Here, 0.3 mM of benzoquinone, ammonium oxalate, and isopropanol were employed as the specific trapping agents to capture superoxide radical ($\bullet O_2^-$), hole (h^+), and hydroxyl radicals ($\bullet OH$), respectively. The subsequent procedures were similar to the above photocatalytic reaction.

3.5. Photoelectrochemical Measurement

The transient photocurrent and electrochemical impedance were measured in a standard three-electrode system on an electrochemical workstation (CH Instrument 660D). The as-synthesized catalyst was dispersed in ethanol with 0.5% Nafion and loaded onto the pre-cleaned fluorine-doped tin oxide conductive glass (FTO) by drop-casting with a surface density of 2 mg/cm^2. The obtained electrode was used as a working electrode, while the Ag/AgCl electrode and platinum wire were employed as the reference and counter electrode, respectively. The electrolyte was 0.2 mol/L of the Na_2SO_4 (pH 7) solution, and a 300 W Xenon lamp (CEL-HXF300) provided the light irradiation. The transient photocurrent was measured at +0.62 V vs. Ag/AgCl with the alternate light on and off every 20 s. Electrochemical impedance spectroscopy (EIS) was examined using a 5 mV amplitude perturbation at a frequency between 100 kHz and 50 mHz. The Mott–Schottky analysis was carried out at 1000 Hz without light illumination. Based on the Nernst equation $E_{RHE} = E_{Ag/AgCl} + 0.059$ pH $+ E^o_{Ag/AgCl}$ (0.197 V), the PEC potential was converted to the reversible hydrogen electrode (RHE) scale, where the pH value was 7.

3.6. Photocatalytic Hydrogen Evolution Measurements

Photocatalytic hydrogen evolution reactions were carried out in a gas-closed circulation system equipped with a vacuum line. A total of 50 mg of photocatalyst was suspended in 100 mL of the 10 vol% methanol aqueous solution (pH 3) in a Pyrex top irradiation reaction vessel equipped with a quartz window. Before turning on a 300 W Xenon lamp (CEL HXF300), the entire reaction system was thoroughly degassed to remove the air. The evolved hydrogen was determined each 30 min by an online gas chromatograph (GC-2030, TET Instrument) equipped with a thermal conductivity detector (5 Å molecular sieve column, He carrier gas, column temperature at 45 °C).

4. Conclusions

In summary, the $CQDs/BiVO_4$ composites were successfully constructed by a facile hydrothermal method, and they exhibited a noteworthy enhancement in the photocatalytic degradation of BzP under visible-light irradiation. Based on the characterization results, CQDs were found to increase the light harvesting of $BiVO_4$ along with the substantially improved charge separation efficiency. Meanwhile, the trapping experiments confirmed that $\bullet O_2^-$ and h^+ were the main active species involved in BzP photodegradation over the $CQDs/BiVO_4$ composite, which were different from that of pristine $BiVO_4$ and resulted from the promoted energy level by CQD modification. Overall, this study offered a new understanding about the CQDs-composited $BiVO_4$ and their photocatalytic properties in eliminating the BzP pollutant.

Supplementary Materials: The following supporting information can be downloaded at: https://www.mdpi.com/article/10.3390/catal13030463/s1, Figure S1: FESEM image of $BiVO_4$; Figure S2: PL spectra of CQDs solution at different excitation wavelength; Figure S3: PL spectra of $BiVO_4$ and $0.6\%CQDs/BiVO_4$; Figure S4: Photocatalytic H_2 evolution of CQDs, $BiVO_4$, $0.6\%CQDs/BiVO_4$, and $0.6\%CQDs/BiVO_4$(mixed).

Author Contributions: Conceptualization, C.H.; Methodology, Q.C., M.T. and W.W.; Project administration, L.C.; Supervision, L.C.; Writing—original draft, C.H.; Writing—review and editing, J.Y. All authors have read and agreed to the published version of the manuscript.

Data Availability Statement: The data presented in this study are available on request from the corresponding author (L.C.).

Conflicts of Interest: The authors declare no conflict of interest.

References

1. Zhu, M.; Sun, Z.; Fujitsuka, M.; Majima, T. Z-scheme photocatalytic water splitting on a 2D heterostructure of black phosphorus/bismuth vanadate using visible light. *Angew. Chem. Int. Ed.* **2018**, *57*, 2160–2164. [CrossRef]
2. Jo, W.J.; Jang, J.-W.; Kong, K.-J.; Kang, H.J.; Kim, J.Y.; Jun, H.; Parmar, K.P.S.; Lee, J.S. Phosphate doping into monoclinic $BiVO_4$ for enhanced photoelectrochemical water oxidation activity. *Angew. Chem. Int. Ed.* **2012**, *51*, 3147–3151. [CrossRef]
3. Parmar, K.P.S.; Kang, H.J.; Bist, A.; Dua, P.; Jang, J.S.; Lee, J.S. Photocatalytic and photoelectrochemical water oxidation over metal-doped monoclinic $BiVO_4$ photoanodes. *ChemSusChem* **2012**, *5*, 1926–1934. [CrossRef]
4. Seabold, J.A.; Choi, K.-S. Efficient and stable photo-oxidation of water by a bismuth vanadate photoanode coupled with an iron oxyhydroxide oxygen evolution catalyst. *J. Am. Chem. Soc.* **2012**, *134*, 2186–2192. [CrossRef]
5. Yuan, D.; Sun, M.; Tang, S.; Zhang, Y.; Wang, Z.; Qi, J.; Rao, Y.; Zhang, Q. All-solid-state $BiVO_4/ZnIn_2S_4$ Z-scheme composite with efficient charge separations for improved visible light photocatalytic organics degradation. *Chin. Chem. Lett.* **2020**, *31*, 547–550. [CrossRef]
6. Xu, X.; Ray, R.; Gu, Y.; Ploehn, H.J.; Gearheart, L.; Raker, K.; Scrivens, W.A. Electrophoretic analysis and purification of fluorescent single-walled carbon nanotube fragments. *J. Am. Chem. Soc.* **2004**, *126*, 12736–12737. [CrossRef]

7.   Wareing, T.C.; Gentile, P.; Phan, A.N. Biomass-based carbon dots: Current development and future perspectives. *ACS Nano* **2021**, *15*, 15471–15501. [CrossRef]

8.   Han, Y.D.; Wu, J.; Li, Y.; Gu, X.Q.; He, T.W.; Zhao, Y.; Huang, H.; Liu, Y.; Kang, Z.H. Carbon dots enhance the interface electron transfer and photoelectrochemical kinetics in TiO_2 photoanode. *Appl. Catal. B Environ.* **2022**, *304*, 120983. [CrossRef]

9.   Wang, Z.; Cheng, Q.; Wang, X.; Li, J.; Li, W.; Li, Y.; Zhang, G. Carbon dots modified bismuth antimonate for broad spectrum photocatalytic degradation of organic pollutants: Boosted charge separation, DFT calculations and mechanism unveiling. *Chem. Eng. J.* **2021**, *418*, 129460. [CrossRef]

10.   Li, H.; Qing, Q.; Zheng, L.; Xie, L.; Gan, Z.; Huang, L.; Liu, S.; Wang, Z.; Lu, Y.; Chen, J. Carbon dots and carbon nitride composite for photocatalytic removal of uranium under air atmosphere. *Chin. Chem. Lett.* **2022**, *33*, 3573–3576. [CrossRef]

11.   Di, J.; Xia, J.; Ji, M.; Wang, B.; Yin, S.; Zhang, Q.; Chen, Z.; Li, H. Carbon quantum dots modified BiOCl ultrathin nanosheets with enhanced molecular oxygen activation ability for broad spectrum photocatalytic properties and mechanism insight. *ACS Appl. Mater. Interfaces* **2015**, *7*, 20111–20123. [CrossRef]

12.   Zhang, Z.; Huang, H.; Xu, J.; Zhang, N.; Zhang, C. Carbon quantum dots/$BiVO_4$ composite with enhanced photocatalytic activity. *Sci. China Technol. Sci.* **2019**, *62*, 356–360. [CrossRef]

13.   Lin, X.; Liu, C.; Wang, J.; Yang, S.; Shi, J.; Hong, Y. Graphitic carbon nitride quantum dots and nitrogen-doped carbon quantum dots co-decorated with $BiVO_4$ microspheres: A ternary heterostructure photocatalyst for water purification. *Sep. Purif. Technol.* **2019**, *226*, 117–127. [CrossRef]

14.   Bolujoko, N.B.; Unuabonah, E.I.; Alfred, M.O.; Ogunlaja, A.; Ogunlaja, O.O.; Omorogie, M.O.; Olukanni, O.D. Toxicity and removal of parabens from water: A critical review. *Sci. Total Environ.* **2021**, *792*, 148092. [CrossRef]

15.   Wei, F.; Mortimer, M.; Cheng, H.; Sang, N.; Guo, L.-H. Parabens as chemicals of emerging concern in the environment and humans: A review. *Sci. Total Environ.* **2021**, *778*, 146150. [CrossRef]

16.   K'Oreje, K.; Okoth, M.; Van Langenhove, H.; Demeestere, K. Occurrence and point-of-use treatment of contaminants of emerging concern in groundwater of the Nzoia River basin, Kenya. *Environ. Pollut.* **2022**, *297*, 118725. [CrossRef]

17.   Xue, J.; Kannan, K. Accumulation profiles of parabens and their metabolites in fish, black bear, and birds, including bald eagles and albatrosses. *Environ. Int.* **2016**, *94*, 546–553. [CrossRef]

18.   Xue, X.; Xue, J.; Liu, W.; Adams, D.H.; Kannan, K. Trophic magnification of parabens and their metabolites in a subtropical marine food web. *Environ. Sci. Technol.* **2017**, *51*, 780–789. [CrossRef]

19.   Yan, W.; Li, M.; Guo, Q.; Li, X.; Zhou, S.; Dai, J.; Zhang, J.; Wu, M.; Tang, W.; Wen, J.; et al. Chronic exposure to propylparaben at the humanly relevant dose triggers ovarian aging in adult mice. *Ecotoxicol. Environ. Safe* **2022**, *235*, 113432. [CrossRef] [PubMed]

20.   Hu, C.; Sun, B.; Tang, L.; Liu, M.; Huang, Z.; Zhou, X.; Chen, L. Hepatotoxicity caused by methylparaben in adult zebrafish. *Aquat. Toxicol.* **2022**, *250*, 106255. [CrossRef]

21.   Hu, C.; Bai, Y.; Sun, B.; Zhou, X.; Chen, L. Exposure to methylparaben at environmentally realistic concentrations significantly impairs neuronal health in adult zebrafish. *J. Environ. Sci.* **2023**, *132*, 134–144. [CrossRef]

22.   Thakkar, S.; Seetharaman, B.; Ramasamy, V. Impact of chronic sub-lethal methylparaben exposure on cardiac hypoxia and alterations in neuroendocrine factors in zebrafish model. *Mol. Biol. Rep.* **2022**, *49*, 331–340. [CrossRef]

23.   Dobbins, L.L.; Usenko, S.; Brain, R.A.; Brooks, B.W. Probabilistic ecological hazard assessment of parabens using *Daphnia magna* and *Pimephales promelas*. *Environ. Toxicol. Chem.* **2009**, *28*, 2744–2753. [CrossRef]

24.   Li, W.; Liu, Y.; Wang, B.; Song, H.; Liu, Z.; Lu, S.; Yang, B. Kilogram-scale synthesis of carbon quantum dots for hydrogen evolution, sensing and bioimaging. *Chin. Chem. Lett.* **2019**, *30*, 2323–2327. [CrossRef]

25.   Miao, R.; Zhang, S.F.; Liu, J.F.; Fang, Y. Zinc-reduced CQDs with highly improved stability, enhanced fluorescence, and refined solid-state applications. *Chem. Mater.* **2017**, *29*, 5957–5964. [CrossRef]

26.   Shi, C.; Qi, H.; Ma, R.; Sun, Z.; Xiao, L.; Wei, G.; Huang, Z.; Liu, S.; Li, J.; Dong, M.; et al. S-self-doped carbon quantum dots from fungus fibers for sensing tetracyclines and for bioimaging cancer cells. *Mat. Sci. Eng. C* **2019**, *105*, 110132. [CrossRef] [PubMed]

27.   Liu, W.; Zhao, G.S.; An, M.Z.; Chang, L.M. Solvothermal synthesis of nanostructured $BiVO_4$ with highly exposed facets and enhanced sunlight-driven photocatalytic properties. *Appl. Surf. Sci.* **2015**, *357*, 1053–1063. [CrossRef]

28.   Park, S.Y.; Lee, H.U.; Park, E.S.; Lee, S.C.; Lee, J.-W.; Jeong, S.W.; Kim, C.H.; Lee, Y.-C.; Huh, Y.S.; Lee, J. Photoluminescent green carbon nanodots from food-waste-derived sources: Large-scale synthesis, properties, and biomedical applications. *ACS Appl. Mater. Interfaces* **2014**, *6*, 3365–3370. [CrossRef]

29.   Zhu, S.; Meng, Q.; Wang, L.; Zhang, J.; Song, Y.; Jin, H.; Zhang, K.; Sun, H.; Wang, H.; Yang, B. Highly photoluminescent carbon dots for multicolor patterning, sensors, and bioimaging. *Angew. Chem. Int. Ed.* **2013**, *52*, 3953–3957. [CrossRef]

30.   Tan, H.L.; Tahini, H.A.; Wen, X.; Wong, R.J.; Tan, X.; Iwase, A.; Kudo, A.; Amal, R.; Smith, S.C.; Ng, Y.H. Interfacing $BiVO_4$ with reduced graphene oxide for enhanced photoactivity: A tale of facet dependence of electron shuttling. *Small* **2016**, *12*, 5295–5302. [CrossRef]

31.   Liu, S.Y.; Li, X.; Meng, X.; Chen, T.X.; Kong, W.Y.; Li, Y.; Zhao, Y.X.; Wang, D.W.; Zhu, S.M.; Cheema, W.A.; et al. Enhanced visible/near-infrared light harvesting and superior charge separation via 0D/2D all-carbon hybrid architecture for photocatalytic oxygen evolution. *Carbon* **2020**, *167*, 724–735. [CrossRef]

32.   Xia, P.F.; Cao, S.W.; Zhu, B.C.; Liu, M.J.; Shi, M.S.; Yu, J.G.; Zhang, Y.F. Designing a 0D/2D S-scheme heterojunction over polymeric carbon nitride for visible-light photocatalytic inactivation of bacteria. *Angew. Chem. Int. Ed.* **2020**, *59*, 5218–5225. [CrossRef]

33. Zhou, H.; Wen, Z.; Liu, J.; Ke, J.; Duan, X.; Wang, S. Z-scheme plasmonic Ag decorated WO_3/Bi_2WO_6 hybrids for enhanced photocatalytic abatement of chlorinated-VOCs under solar light irradiation. *Appl. Catal. B Environ.* **2019**, *242*, 76–84. [CrossRef]

34. Huang, Y.; Liang, Y.; Rao, Y.; Zhu, D.; Cao, J.-J.; Shen, Z.; Ho, W.; Lee, S.C. Environment-friendly carbon quantum dots/$ZnFe_2O_4$ photocatalysts: Characterization, biocompatibility, and mechanisms for NO Removal. *Environ. Sci. Technol.* **2017**, *51*, 2924–2933. [CrossRef]

35. Hu, C.; Tian, M.; Wu, L.; Chen, L. Enhanced photocatalytic degradation of paraben preservative over designed g-C_3N_4/$BiVO_4$ S-scheme system and toxicity assessment. *Ecotoxicol. Environ. Safe* **2022**, *231*, 113175. [CrossRef]

36. Yu, J.; Zhang, Y.; Li, H.; Wan, Q.; Li, Y.; Yang, N. Electrochemical properties and sensing applications of nanocarbons: A comparative study. *Carbon* **2018**, *129*, 301–309. [CrossRef]

37. Liang, L.L.; Gao, S.W.; Zhu, J.C.; Wang, L.J.; Xiong, Y.N.; Xia, X.F.; Yang, L.W. The enhanced photocatalytic performance toward carbamazepine by nitrogen-doped carbon dots decorated on $BiOBr$/CeO_2: Mechanism insight and degradation pathways. *Chem. Eng. J.* **2020**, *391*, 123599. [CrossRef]

38. Liu, B.; Yin, D.; Zhao, F.; Khaing, K.K.; Chen, T.; Wu, C.; Deng, L.; Li, L.; Huang, K.; Zhang, Y. Construction of a novel Z-scheme heterojunction with molecular grafted carbon nitride nanosheets and V_2O_5 for highly efficient photocatalysis. *J. Phys. Chem. C* **2019**, *123*, 4193–4203. [CrossRef]

39. Kuang, Y.; Jia, Q.; Ma, G.; Hisatomi, T.; Minegishi, T.; Nishiyama, H.; Nakabayashi, M.; Shibata, N.; Yamada, T.; Kudo, A. Ultrastable low-bias water splitting photoanodes via photocorrosion inhibition and in situ catalyst regeneration. *Nat. Energy* **2016**, *2*, 16191. [CrossRef]